Implementation of Noise Spectroscopy Using Biased Large-Area Photodiodes

Willem G. J. Langeveld, Cathie Condron, Mashal Elsalim, Peter Grudberg, Victor Hu, Peter Ryge, *Member, IEEE*, Tim Shaw, and Shrabani Sinha

***Abstract*—The bremsstrahlung X-ray spectrum produced by X-ray sources used in cargo inspection systems is attenuated and modified by materials in the cargo in a Z-dependent way and then detected in a radiographic detector array. We have previously shown that it is possible to obtain spectral information indirectly by analyzing statistical fluctuations (the "noise") in radiographic data, in a technique we call Noise Spectroscopy (NS) or Z-SCAN (Z-determination by Statistical Count-rate ANalysis). The technique is especially effective when the detector array consists of fast scintillation detectors and waveform digitization electronics, measuring both the waveform mean and variance during each X-ray pulse. This previous work, however, used photo-multiplier tubes, which are not especially suitable for a practical implementation. Here we describe the results of R&D performed to produce an effective version of the technique that lends itself to implementation in a single detector array that can be used both for radiography and for NS, with the same imaging spatial resolution as in conventional systems. We characterize the performance of biased photodiodes in combination with trans-impedance preamplifiers, read out with commercially available waveform digitizers. We report on experiments performed with a 16-channel detector array in a test beam, with test samples of different atomic number Z. We also report the implementation of an NS algorithm in an FPGA. In combination, we show that a practical implementation of Noise Spectroscopy in cargo inspection systems is feasible.**

***Index Terms*—Cargo inspection, noise spectroscopy, statistical methods, waveform analysis, X-ray radiography, X-ray spectroscopy, Z-determination by statistical count-rate analysis, Z-SCAN.**

I. Introduction

In high-energy (4–10 MeV) X-ray cargo imaging, material discrimination can be accomplished using existing techniques, the most common of which is dual-energy X-ray imaging [1]. In dual-energy X-ray imaging, alternating pulses of the X-ray source are produced with a low-energy or high-energy electron beam, e.g. 4 MeV and 6 MeV, or 6 MeV and 9 MeV. Dual-energy sources, however, have disadvantages:

- the pulse stability from one pulse to the next of the same energy is not nearly as good as for single-energy sources;
- the energy calibration of commercial sources is usually not very well known: experience has shown considerable variability from one source to another;
- the system imaging penetration is limited to that achievable with the lowest of the two energies;
- two X-ray pulses are needed for material discrimination, one at low energy and one at high energy, to make one column of pixels in the image. In order to maintain spatial resolution in the scan direction, dual-energy sources therefore need twice as many pulses;
- since the cargo can move appreciably with respect to the system between the two pulses, image artifacts can result, especially on vertical boundaries.

Noise spectroscopy (NS) was introduced [2] as an alternative method, which uses statistical analysis of the detector signal during each X-ray pulse. NS has the following advantages:

- one can use single-energy source, which is less expensive, and pulse-to-pulse stability is much better;
- one can always run at the highest energy supported by the source, and the imaging penetration is not limited by the lower of the two energies;
- there is no need for twice the number of pulses. The system has the same spatial resolution as a non-NS-enabled system;
- there are no image artifacts since material discrimination is based on data from a single pulse of the X-ray source.

In production, system costs may not be very different from a dual-energy system: the detectors and electronics might be more expensive, but a single-energy source is considerably more economical.

Noise Spectroscopy (also known as Z-SCAN: Z-detection by Statistical Count-rate ANalysis) is based on the fact that the spectrum of x rays is changed by the material they penetrate in a way that depends on the atomic number, Z, of the material, due primarily to Compton scattering at low energies and pair-production at high energies. Fig. 1 shows the (calculated and normalized) spectra of unattenuated and attenuated x rays. From left to right, we show the unattenuated original bremsstrahlung spectrum, and the attenuated spectra for 10 cm of lead, 20 cm of iron, and 89 cm of carbon. These thicknesses lead to about the same signal in the imaging detector array of a system when a

Manuscript received June 15, 2012; revised August 16, 2012; accepted October 01, 2012. Date of publication December 11, 2012; date of current version April 10, 2013. This work has been supported by the U.S. Department of Homeland Security, Domestic Nuclear Detection Office, under competitively awarded contract(s)/IAA(s) HSHQDC-10-C-00170. This support does not constitute an express or implied endorsement on the part of the Government.

W. G. J. Langeveld, C. Condron, M. Elsalim, T. Shaw, and S. Sinha are with Rapiscan Laboratories, Inc., Sunnyvale, CA, 94085 USA (e-mail: wlangeveld@rapiscansystems.com).

P. Grudberg is with XIA LLC, Hayward, CA, 94544 USA (e-mail: peter@xia.com).

V. Hu is with Victor Hu Consulting, Palo Alto, CA, 94304 USA (e-mail: hu8743@comcast.net).

P. Ryge is with Peter Ryge Consulting, Carlsbad, CA, 92009 USA (e-mail: peterryge@yahoo.com).

Color versions of one or more of the figures in this paper are available online at http://ieeexplore.ieee.org.

Digital Object Identifier 10.1109/TNS.2012.2223485

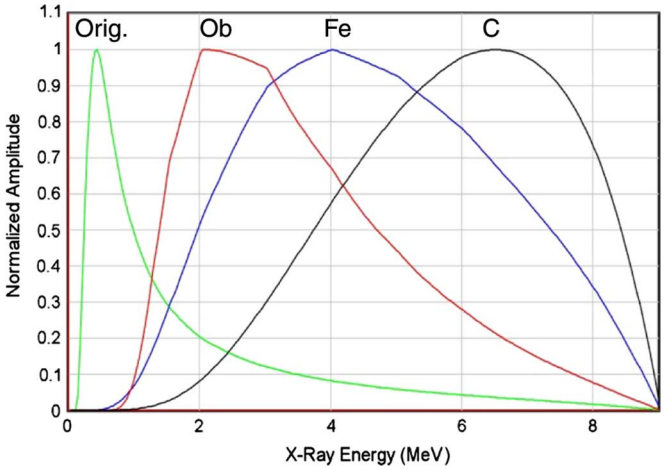

Fig. 1. Normalized spectra behind 8 in. steel-equivalent (SE) of materials of different Z, compared to the original bremsstrahlung spectrum.

9 MV X-ray source is used. We can therefore say, for example, that 10 cm of lead is about 20 cm steel-equivalent (SE).

From Fig. 1 we see that lower-Z materials lead to harder spectra (higher average X-ray energies) and higher-Z materials lead to softer spectra (lower average X-ray energies). This then leads to a statistical effect: the variance of the measured signal is higher for low-Z materials and lower for high-Z materials. If we designate the signal in any given detector by S, we have

$$S = \alpha \langle E \rangle N \tag{1}$$

with $\langle E \rangle$ the average energy deposited by the x rays, N the number of x rays, and α a constant depending on detector efficiency and read-out system. In this discussion we will assume that α does not depend on X-ray energy. The variance is

$$\mathrm{var}(S) = \alpha^2 \langle E^2 \rangle N \tag{2}$$

with $\langle E^2 \rangle$ the average deposited energy-squared of the x rays. We can then define the noise figure, Y, as

$$Y = \frac{\mathrm{var}(S)}{S} = \frac{\alpha \langle E^2 \rangle}{\langle E \rangle}. \tag{3}$$

Note that Y only depends on quantities determined by the X-ray energy spectrum and, aside from a calibration constant, has dimensions of energy.

The Noise Spectroscopy method, then, consists of determining Y in addition to the signal S. The technique can therefore be said to be based on the Campbell theorem [3]. The method also bears some similarity to the Feynman-Y (or Feynman-α) method for nuclear fission analysis [4], but the Feynman Y relates to variations in the *number* of, in that case, neutrons, not their number *and* energies.

Starting from bremsstrahlung spectra, we can compute the spectra behind quantities of materials of different Z using the standard NIST mass attenuation coefficients [5], and compute the noise figure Y. In Fig. 2 we plot Y versus the transmission (with α set to 1) for a number of materials and material thicknesses. The transmission t is defined as the observed signal S

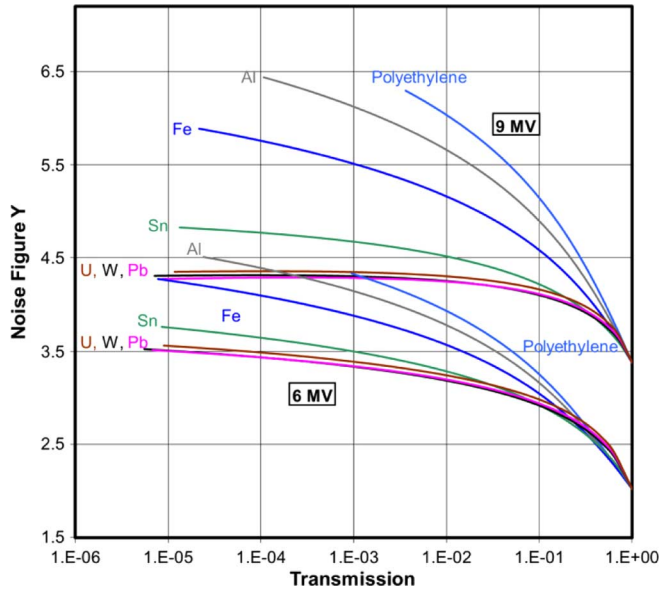

Fig. 2. Y versus transmission for 7 different materials. Calculations for 9 MV source energy are shown in the upper curves, those for 6 MV source energy in the lower curves. The dispersion for 9 MV is much larger than for 6 MV. Materials with a Z $>\sim$ 70 cannot easily be distinguished from one another.

in the detector divided by the signal the detector would see without attenuating material, S_{air}

$$t = \frac{S}{S_{\mathrm{air}}}. \tag{4}$$

S_{air} is usually measured as part of calibration data at the beginning and/or end of a scan. Alternatively, the signal of a reference detector can be used.

We see from Fig. 2 that high-Z materials have low values of Y and low-Z materials have high values of Y. We also see that the method has better material separation with a high-energy X-ray source (e.g., 9 MV—upper curves) than with a low-energy source(e.g., 6 MV—lower curves). Materials of the same steel-equivalent thickness (in cm SE) by definition show the same transmission value in the detector, but determination of the variance in the signal allows computing Y and, hence, determining the (average) Z of the material. We further observe that materials with a Z much higher than that of tin (Z $= 50$) cannot easily be distinguished from one another.

Implementation into a cargo inspection system requires fast scintillators, photo-detectors, preamplifiers, and digitization electronics. Whereas it is important that the detectors have some energy resolution, that resolution does not have to be very good: as long as there is an approximate proportionality between the X-ray energy and the resulting detector signal, the method will work.

In order to avoid large data transfers, it is desirable to compute the signal and variance in the firmware of the digitization hardware for each detector element, and deliver to the central computer system only the signal and its variance.

The detector signals are aggregated on a central processor to form a radiographic image, usually producing one column of pixels in the image for each X-ray pulse. A segmentation algorithm designates pixels belonging to the same object and

those belonging to the background. An average noise figure is then determined for each object, using a background-subtracted value for the signal. The result is then compared to calibrated values and the material Z is determined.

The uncertainty δY in the noise figure defined by (3) is determined primarily by the uncertainty in the variance. If we have a number of samples S, the variance of the sample variance is given by, e.g., [6] as: $2\,\mathrm{var}(S)^2/N$, with N the number of measurements of S. Thus, we can approximate

$$\mathrm{var}(Y) = \mathrm{var}\left(\frac{\mathrm{var}(S)}{S}\right) \approx \frac{S^{-2}2\mathrm{var}(S)^2}{N} = \frac{2Y^2}{N} \tag{5}$$

or

$$\delta Y \approx Y\sqrt{\frac{2}{N}}. \tag{6}$$

Whereas, (6) is only approximately correct, it does show that the accuracy of the determination of the noise figure grows with the square root of the number of measurements of the signal S. Therefore, the signal should be measured as often as possible, which naturally suggests sampling the signal during the X-ray pulse. This then leads to the requirement for fast detectors and electronics.

In [2] we demonstrated the effect using a photomultiplier tube (PMT). PMTs, however, are too large to be usable in a linear array of detectors with a pitch as low as 5 mm. They are also rather fragile for use in a mobile system. For these reasons, a solid state solution is preferred.

The elements of a practical implementation and tests performed are described in the following sections.

II. Detectors, Electronics, and Data Collection

A. Scintillators and Reflectors

Typical cargo inspection systems use $CdWO_4$ for their scintillators and unbiased PIN photodiodes for their photo-detectors, and integrate over the entire X-ray pulse. These are too slow for the purposes required here: $CdWO_4$ has a decay time of $\sim$15 μs, which is longer than the X-ray pulse duration of most linac X-ray sources. In [2], we demonstrated that LYSO (Lutetium Yttrium Ortho-Silicate) with its 40 ns decay time is a suitable alternative. The crystals used here are 11.35 mm $\times$ 11.35 mm $\times$ 25 mm in size.

Extensive optical simulations were performed using an in-house optical simulation code and with the well-known DETECT2000 program [7] to optimize the light collection efficiency of the LYSO crystals, which have an emission peak at 420 nm. A configuration that was found to have good light yield (>60%) has all scintillator faces ground except for a polished face to which the photodiode was glued using Epotek 301-2 epoxy (see Fig. 3). The assembly was then wrapped in Tyvek, keeping an air gap, and surrounded by copper tape in order to shield the photodiode from electronic noise pickup. The copper tape was later grounded. The simulations showed further that the light collection uniformity is very good for this configuration.

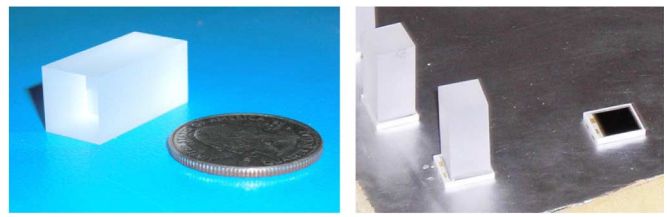

Fig. 3. LYSO crystals and Hamamatsu S3590-18 photodiodes in the process of being glued together.

Since optical simulations are notoriously somewhat qualitative in nature, we intend to study this configuration (and others) further in the future.

B. Photo-Detectors

In [2], feasibility of NS was shown using a photo-multiplier tube. We report here that the same can be accomplished with PIN photodiodes as well, if a bias voltage is applied. This considerably decreases the rise and decay times and lowers the capacitance. We obtained large-area ($\sim$ 100 mm^2) photodiodes from several manufacturers. We tested them for red and blue response, rise time and signal FWHM, electronics noise performance and overall pulse height. All photodiodes performed best at the highest recommended bias voltages. Whereas several photodiodes had adequate performance, Hamamatsu photodiodes stood out in almost every respect. Eventually, we selected the Hamamatsu S3590-18 for this project. The other photodiodes would have likely worked as well, but they yielded significantly smaller signals.

C. Preamplifiers

Because of the relatively high capacitance of large-area photodiodes, it is important to couple them to a trans-impedance preamplifier in order to yield an adequate time response [8]. The circuit diagram for the preamp used here is shown in Fig. 4. The right-hand part of the circuit is a two-pole noise filtration circuit. The overall bandwidth of this circuit is about 40 MHz.

Four preamplifier boards were made with 4 channels each of this circuit.

D. Digitization Electronics

The data presented in the following sections were acquired using a DGF Pixie-4 multichannel data acquisition system supplied by XIA LLC, consisting of a chassis with a computer and four four-channel Pixie-4 modules. After a digitally controlled gain and offset stage, signals are digitized in a 14-bit ADC at a rate of 75 MHz. An external trigger was provided in the experiments. XIA provided custom firmware to write waveforms to the hard drive of the system.

XIA also developed custom firmware to implement an NS algorithm in an XIA STJ module. The STJ module is a PXI digital pulse processor with 32 12-bit ADC channels at 50 MSPS, and two Spartan-6 FPGAs. One of the NS algorithms (see later) was implemented in firmware and tested, but not used in the experiments reported here. In order to ensure sufficient dynamic range, we plan to use two ADC channels for each detector, each with a different gain, in future experiments.

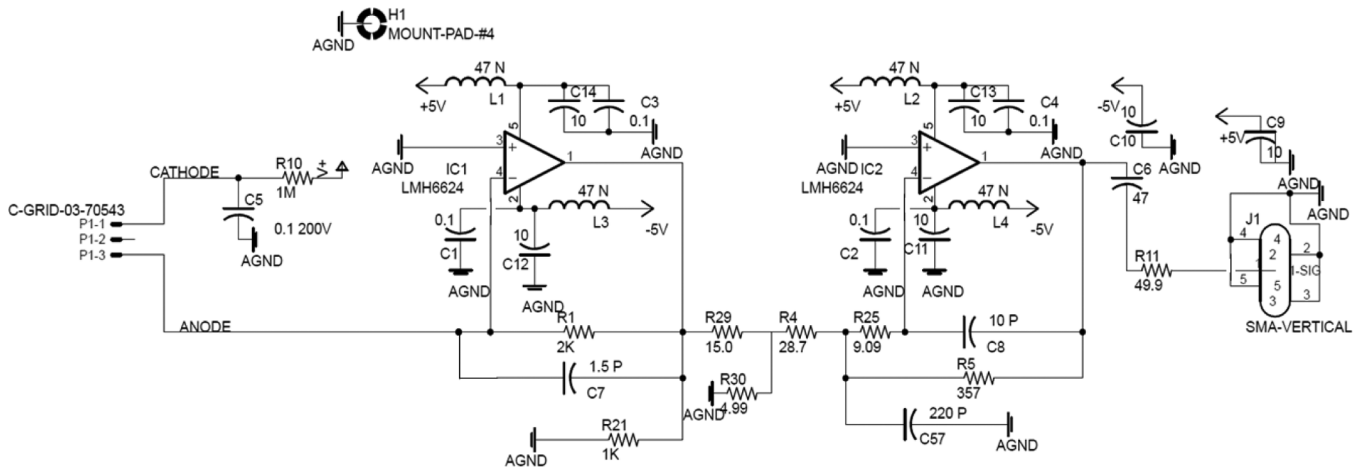

Fig. 4. Trans-impedance preamplifier circuit with two-pole noise filter.

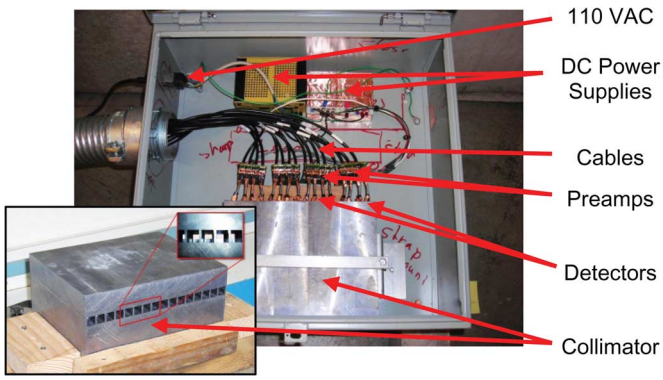

Fig. 5. 16-Channel test array, with Pb collimator (inset).

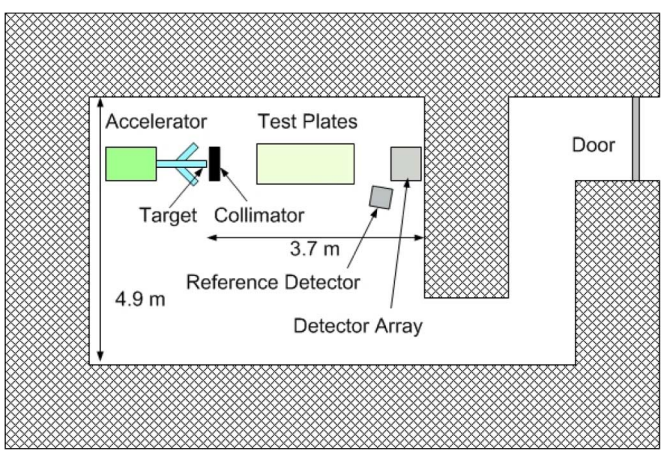

Fig. 6. Layout of the test facility.

E. Test Array

Using the components discussed above, a 16-channel detector array was assembled in a light-tight box (see Fig. 5). The detector elements were inserted into a lead collimator, which has lead septa between individual detector elements.

The center-to-center spacing between subsequent detector mounting holes is 12.5 mm. To fit the geometry of the test cell, the focus distance of the collimator is ~4 meters.

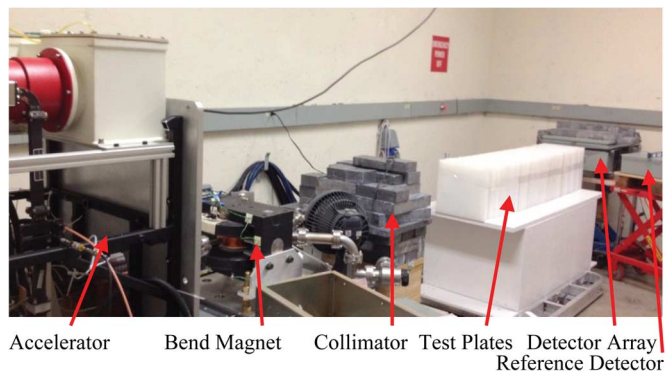

Fig. 7. Photograph of the setup.

F. Test Setup

Tests were performed in a test cell at Accuray, Inc., in their test facilities in Mountain View, CA. The Accuray X-ray source is a good quality source with a wide X-ray pulse ($\sim 4.5\ \mu$s) and the pulse-to-pulse stability was adequate. The Accuray system has a bend magnet, allowing determination of the beam energy. The accelerator properties tended to change a little between runs, and also sometimes within runs, but this was only a minor problem.

A reference detector was built by taking one of the detectors from the main array and a spare preamp circuit, mounted with its own lead collimator in a separate light-tight box, positioned so as to have an unobstructed view of the x ray source.

A lead source collimator was built to reduce the amount of scattered x rays from the otherwise unshielded source. Remaining scatter from the source was reduced by surrounding the detector array with lead.

Test plates of 30 × 30 cm size were acquired in 7 different materials: 60 1-inch-thick plates of polyethylene (“Poly”), 30 1 1/2-inch plates of aluminum (Al), 64 1/4-inch plates of steel (Fe), 64 1/4-inch plates of tin (Sn), 31 1/4-inch plates of tungsten (W) and 36 1/4-inch plates of lead (Pb). We use units of inches since they are commonly used in the cargo inspection industry.

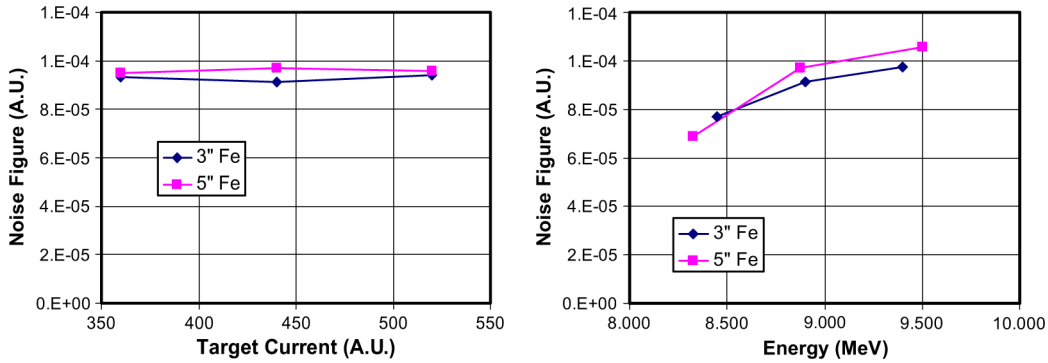

Fig. 8. Noise figure sensitivity to variations in beam intensity (left) and beam energy (right).

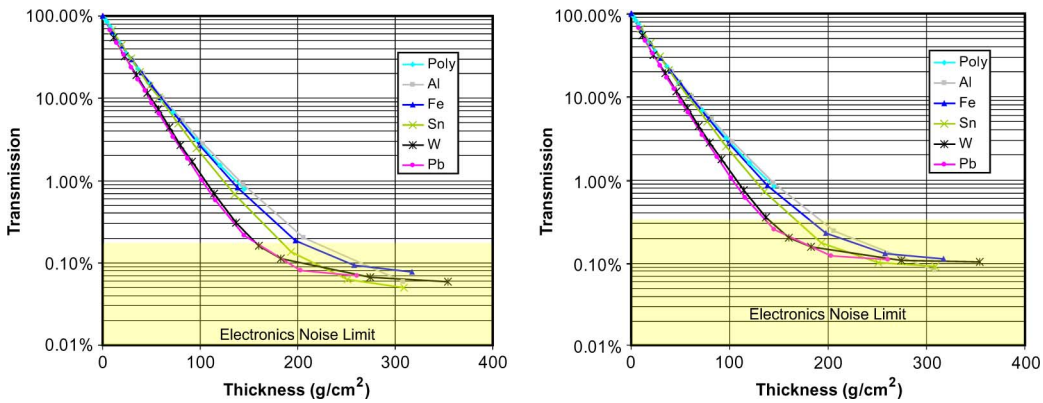

Fig. 9. Transmission versus material thickness (in $\mathrm{g/cm^3}$) for two detectors. The detector represented by the graph on the left shows higher transmission capability. The highlighted areas show the extent of the electronics noise.

G. Data Collection

Data were collected for almost three weeks. The data quality was generally very good. In addition to many runs with different amounts and different types and combinations of materials, several runs were performed to determine the stability of the system with regard to current and energy variations of the X-ray source. It was found that beam current did not influence the results, but beam energy variations did, see Fig. 8. This is as expected from (3) and Fig. 2.

We found that not all detectors have the same behavior. This is shown, for example, in Fig. 9, where transmission data are plotted for two detectors. The left-hand plot shows better performance than the right-hand plot, as is evidenced by the lower transmission floor. This may be due to differences in electronics noise between the two channels, or perhaps one detector saw more X-ray scatter from the source than the other. We further observed that, despite the fact that all detectors are calibrated to give the same signal value at a given source intensity, material type and thickness, there are differences in the noise figures obtained from different detectors that would need to be calibrated out in a final system. Mostly this difference consists of an offset; otherwise the data from different detectors are quite comparable.

Fig. 10 shows the transmission versus material thickness, with exponential fits to the data. Deviations from the fit are due to beam hardening: the energy spectrum changes as the x rays traverse the material, becoming more energetic and better able to penetrate the material, leading to the nonexponential behavior seen in the figure. From the fits, the steel-equivalency of the materials can be derived; see Table I.

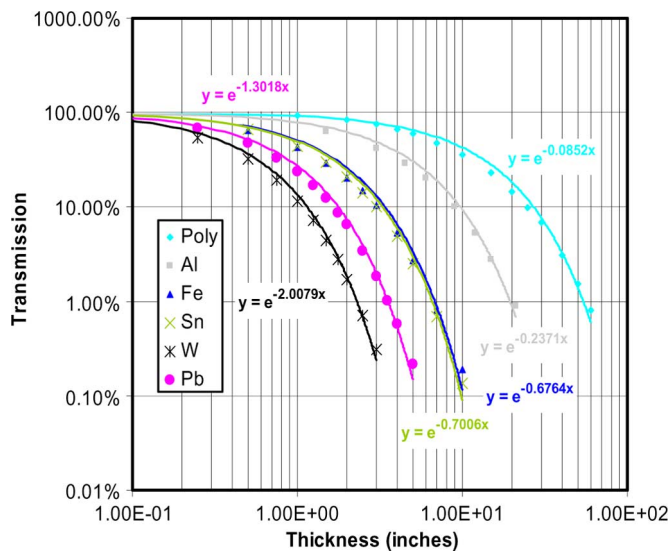

Fig. 10. Transmission versus thickness (inches) as measured using a single detector. The lines are exponential fits.

III. Algorithms and Results

Two algorithms were designed; algorithm 1 uses the reference detector, and algorithm 2 does not (except to determine the transmission). Both algorithms were tested offline in software.

TABLE I
MATERIAL THICKNESS EQUIVALENCIES

Material	Symbol	Z	Density (g/cm^3)	1" Material Equals[c]	1" Steel Equals[c]
Poly	$(CH_2)_n$	~2.5	0.9	0.126" Fe	7.937"
Aluminum	Al	13	2.7	0.350" Fe	2.857"
Steel	Fe[a]	26	7.9	1.000" Fe	1.000"
Tin	Sn	50	7.3	1.033" Fe	0.968"
Tungsten	W	74	~18[b]	2.966" Fe	0.337"
Lead	Pb	82	11.4	1.923" Fe	0.520"

[a] The hot-rolled steel plate used in this program is ~98% Fe.
[b] The tungsten used is a 95% W alloy produced per ASTM B777 Class 3.
[c] Units of inches are used here because they are commonly used in the cargo inspection industry. Since inches are compared to inches in this table, the conversion factors are numerically the same for any unit system.

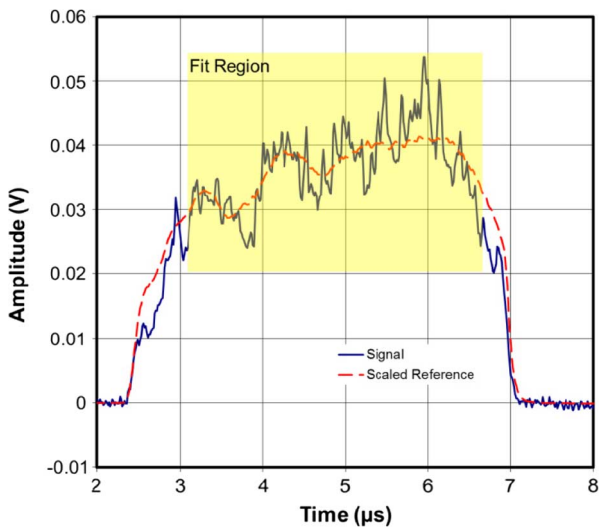

Fig. 11. Test waveform behind 15 inches of Aluminum (solid line), with scaled reference waveform (dashed line) after the fit. The highlighted region shows the time region used in the computation of the χ^2 of the fit.

Algorithm 1 consists of the following procedure. The (offset-subtracted) signal waveform in a detector from the 16-channel test array ("test waveform") is digitized over the duration of one X-ray pulse. Similarly, the signal waveform in the reference detector ("reference waveform") is digitized over that same X-ray pulse. We use the reference waveform as a proxy of the average waveform produced by the accelerator. A fit is made of the reference waveform to the test waveform, using a fixed time region of the pulse, with an amplitude coefficient multiplying the reference waveform as the single free parameter. An example of such a fit is shown in Fig. 11: the solid line shows the test waveform from one of the detectors of the array, with 15 inches of Aluminum as a test sample. The dashed line shows the scaled reference waveform after the fit. The highlighted area covers the time region used for the fit. The χ^2 of the fit is the sum of the squares of the deviations of the test waveform with respect to the reference waveform. The formula for the χ^2 is therefore similar to what one would use to compute the variance of the signal with respect to the average waveform. The noise figure is then estimated by dividing the χ^2 by the total signal integral.

This is done for some number, N, of test waveforms, each of which can be taken as a separate "pixel" in a hypothetical image of a cargo consisting of the test material. The noise figure,

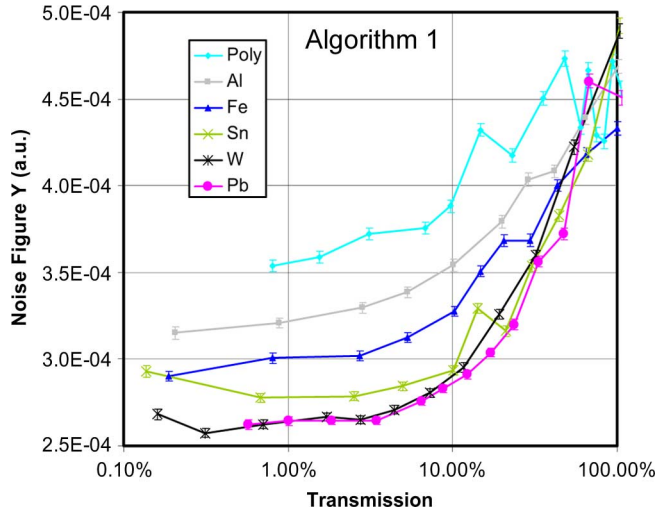

Fig. 12. Noise figure versus transmission for algorithm 1, averaged over the equivalent of $N = 500$ pixels. The error bars include only statistical uncertainties.

Y, averaged over N such pixels, is used as the best estimate, and the uncertainty in this average, δY, is determined from the standard deviation σ of the measured noise figures using the usual formula for the error in the mean: $\delta Y = \alpha/\sqrt{N}$.

Algorithm 1 works especially well for low-transmission data, but not as well for data with transmission >10%; see Fig. 12. One reason may be that the "noise" in the reference waveform contributes to the noise figure from the test waveform, especially where the test waveform is large enough to be comparable to the reference waveform. Since the algorithm requires the reference waveform to be available at the same time as the test waveform, this algorithm is difficult (though not impossible) to implement in the firmware of the digitizer channel of each detector in the array.

Thus far, we have obtained the noise figure, more or less directly, from the digitized test waveform. At a sample rate of 75 MSPS each sample covers 13.3 ns. The time resolution of the detector array, however, is determined by the decay time of the scintillator and by the response time of the read-out hardware, which totals some 50–60 ns. It is therefore better to average the data, for example by smoothing each data sample S_j using the formula

$$\overline{S}_i = \sum_{j=i-n}^{i+n} \frac{S_j}{2n+1} \tag{7}$$

for some value of n. For the test waveform we might use, for example, $n = 2$, causing the signal to be averaged over 5 time bins. In Algorithm 2, we also use (7) to make an estimate of the average waveform, by using a larger value of n, for example $n = 8$. The original test waveform (i.e., $n = 0$) is shown, together with the $n = 8$ average waveform, in Fig. 13. We "fit" (this time with no free parameters) this $n = 8$ average waveform to the $n = 2$ test waveform in a fixed time region (yellow area in Fig. 13). As before, the χ^2 is a good estimate of the signal variance and the same procedure is used to obtain the noise figure averaged over a number N of pixels.

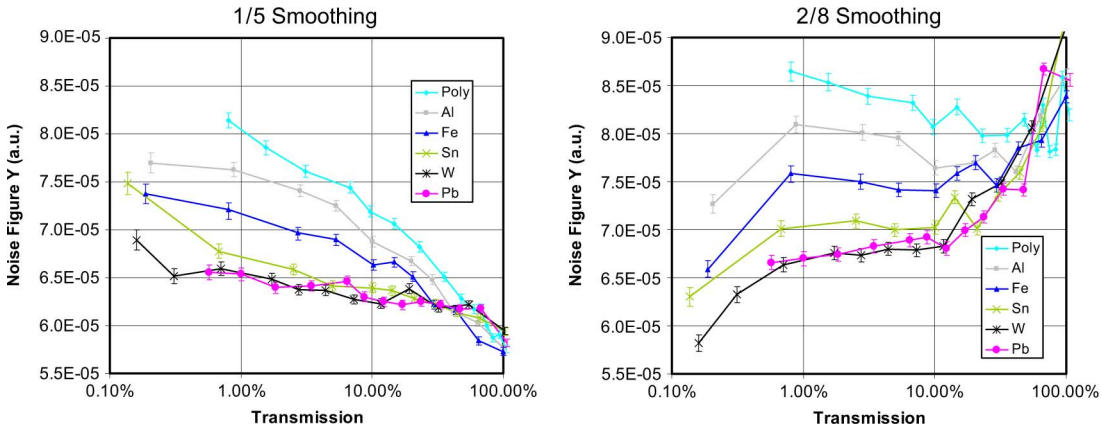

Fig. 14. Measured noise figures versus transmission for two different smoothing settings, averaged over the equivalent of 500 pixels. On the left (right), $n = 1$ ($n = 2$) was used to estimate the test waveform, and $n = 5$ ($n = 8$) was used to estimate the average waveform. The error bars include only statistical uncertainties.

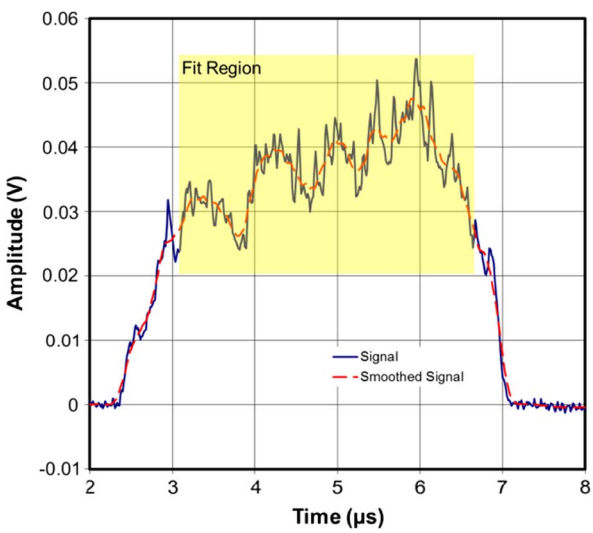

Fig. 13. Test waveform behind 15 inches of Aluminum, with average waveform (using $n = 8$). The highlighted area shows the time region used in the computation of the χ^2.

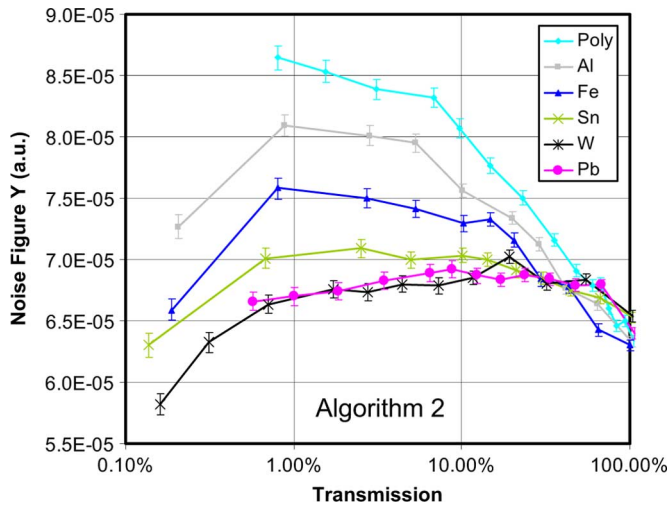

Fig. 15. Combination of the algorithms used in Fig. 14: above 10% transmission we use $n = 1$ and 5 smoothing, and below 10% transmission we use $n = 2$ and 8 smoothing. The noise figures above 10% were also multiplied with a fixed number in order to match them to the values below 10% transmission. The error bars include only statistical uncertainties.

Algorithm 2 works well for low-transmission data, and it can work well for data with transmission >10%, depending on the values of n. For example (see Fig. 14), using $n = 1$ for "test" and $n = 5$ for "average" yields good results above 10% transmission, whereas $n = 2$ for "test" and $n = 8$ for "average" yields better results below 10% but worse results above 10%.

In the end, we use a combination of the two, see Fig. 15. Above 10% transmission we use values of $n = 1$ and 5 and below 10% transmission we use values of $n = 2$ and 8. The noise figures for transmission >10% were also multiplied with a fixed number in order to match them to the values below 10% transmission. Overall, algorithm 2 is usable up to about 30% transmission. Above 30% transmission, material discrimination is difficult for both algorithms. An advantage of algorithm 2 is that calculation of χ^2 does not require the availability of reference detector data, and hence is much more easily implemented in the firmware of the digitization hardware.

IV. Detection of High-Z Objects

The results shown thus far were derived assuming "objects" in the "cargo" that span an area of about $N = 500$ pixels, or about 23 pixels × 23 pixels. For the detector size used here, the spatial resolution is on the order of 5–6 mm per pixel, assuming the object is halfway between the source and the detector array, i.e. the corresponding object size would be about 13 cm × 13 cm. In particular, objects of Special Nuclear Materials (SNM) shielded with high-Z materials might have about that size [1]. Fig. 15 shows that the material separation for such large objects is excellent below about 20–30% transmission, and these objects would actually have a transmission very much less than that.

The method also works for smaller objects, but of course with lower fidelity. Fig. 16 shows the results for an "object" with only 80 pixels ($\sim 9 \times 9$ pixels), which translates to a size of about 5 cm × 5 cm. Such sizes could correspond to small SNM objects that are unshielded or shielded with lower-Z materials. From

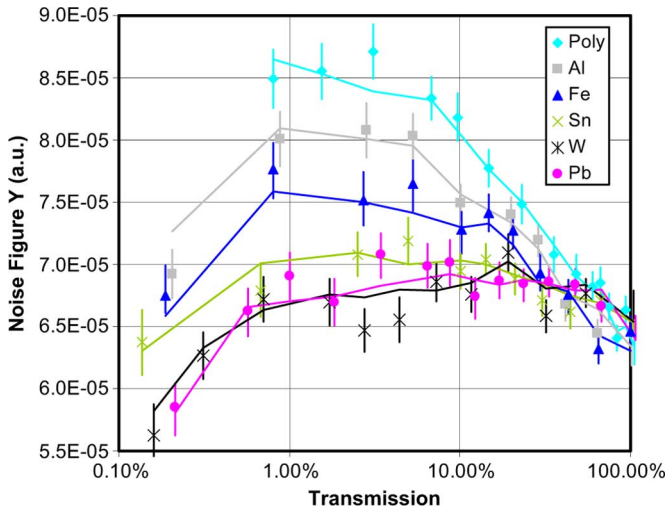

Fig. 16. Algorithm 2 applied to the equivalent of about 80 pixels (points with error bars). The lines are taken from Fig. 15 to guide the eye. Note that some of the scatter of the data points is due to run-to-run differences.

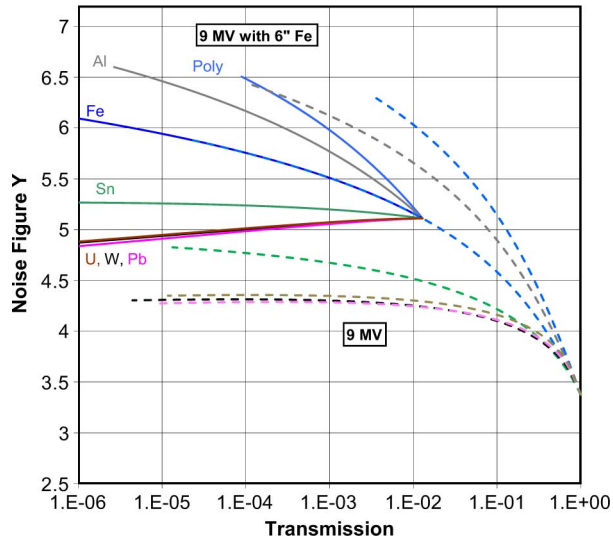

Fig. 17. Calculated noise figures versus transmission for various materials with a shield of 6 inches of steel. For comparison, the noise figures from Fig. 2 without the additional steel are shown with dashed curves.

Fig. 16 it is clear that such high-Z objects, which would have a transmission below about 2%, would easily be distinguished from steel and lower-Z materials, but not from materials with a Z around that of tin.

When multiple materials of different Z overlap each other in an image, the NS method would, of course, yield some average noise figure Y_{total} for the combination of materials

$$Y_{\text{total}} = \frac{\text{var}(S_{\text{total}})}{S_{\text{total}}} \tag{8}$$

with S_{total} the total measured signal and $\text{var}(S_{\text{total}})$ the measured variance.

SNM can be shielded with high-Z or low-Z shielding materials. If the object is largely shielded with high-Z materials, the total noise figure would be mostly that of a high-Z material, which would justify an alarm all by itself.

If a suspected SNM object (or, more generally, SNM shielded with high-Z materials) is shielded with lower-Z materials, it is still possible to determine the Z for the suspected object. The shield would necessarily cover a significantly larger area in the image than the object itself in order to shield it in all directions, since it is not probable that the cargo scanning geometry can be predicted. The transmission of the shield can then be determined by examining the image around the boundary of the object (after image segmentation). The transmission of the shield

$$t_{\text{shield}} = \frac{S_{\text{shield}}}{S_{\text{air}}} \tag{9}$$

can be taken as the average transmission of pixels outside this boundary. The total unsubtracted transmission at the location of the object itself is given by

$$t_{\text{total}} = \frac{S_{\text{total}}}{S_{\text{air}}}. \tag{10}$$

Similarly, the noise figure of the signal due to the shield Y_{shield} is determined, by averaging the noise figures of pixels outside the boundary. This establishes the extent and type of shielding, and one can look up the Z of the shield by interpolation, using calibrated noise figure values.

Fig. 17 shows what happens to the noise figure for a situation where various materials in various thicknesses are also shielded with 6 inches of steel. The noise figure is still clearly different for different materials, but if it is not known there is a shielding material, one can only rely on the curves calculated without the shield (dashed curves in Fig. 17) and one will generally obtain some average value for the Z of the material.

But if the presence of shielding is known or suspected, the procedure to determine the noise figure of the object is as follows. First one determines the transmission t_{shield} and noise figure Y_{shield} of the shield. In the example of Fig. 17, this corresponds to the location at about (1E-02, 5) in the Figure. This yields the Z of the shield Z_{shield} by interpolation between the dashed curves (or, more likely, a tabulated version thereof). Then the energy spectrum behind the shield is calculated assuming a spectral filter made of material with $\text{Z} = \text{Z}_{\text{shield}}$ in an amount that would yield t_{shield} by itself. A new plot of noise figure versus transmission, i.e. Fig. 17 in the example, can then be prepared using the filtered energy spectrum. The noise figure Y_{total} together with transmission t_{total} can now be properly interpreted, and the Z of the object can be derived.

Many of these computations can be done once and stored in various tables for easy lookup in a deployed system.

V. Conclusion

A proof-of-concept small detector array implementing Noise Spectroscopy in a practical manner was built and tested in a test beam with a 9 MV X-ray source, demonstrating feasibility of the approach. The elements of the implementation consisted of biased large-area photo-diodes as a suitable fast (non-PMT) photo-detector that can be coupled to LYSO as a fast enough scintillator material; trans-impedance preamplifiers to read out the photodiodes, with low enough noise and high enough speed to enable radiography and NS in a single detector array; and

digitization electronics to capture the X-ray pulse waveform at a high enough level of accuracy with a noise spectroscopy algorithm in firmware.

In future work, we intend to produce a larger set of detector modules and test it in an existing cargo imaging system.

REFERENCES

[1] R. Bentley, "Database of high-Z signatures in cargo," in *Proc. IEEE Int. Conf. Technol. Homeland Security (HST)*, Waltham, MA, 2011, pp. 379–383.

[2] W. G. J. Langeveld, C. Condron, M. Elsalim, and M. Ingle, "Noise spectroscopy: Z-determination by statistical count-rate analysis (Z-SCAN)," *Nucl. Inst. Meth. A*, vol. A 652, pp. 79–83, 2011.

[3] N. R. Campbell and V. J. Francis, "A theory of valve and circuit noise," *JIEE*, vol. 93, no. 3, 1946.

[4] R. P. Feynman, F. DeHoffman, and R. Serber, "Dispersion of the neutron emission in U-235 fission," *J. Nucl. En.*, vol. 3, pp. 64–69, 1956.

[5] J. H. Hubbell and S. M. Seltzer, Tables of X-ray Mass Attenuation Coefficients and Mass Energy-Absorption Coefficients [Online]. Available: http://www.nist.gov/pml/data/xraycoef/index.cfm National Institute of Standards and Technology. Gaithersburg, MD.

[6] Y. Bar-Shalom, X. RongLi, and T. Kirubarajan*, Estimation With Applications to Tracking and Navigation*, 1st ed. Hoboken, NJ: Wiley, 2001, pp. 106–107.

[7] F. Cayouette, D. Laurendeau, and C. Moisan, "DETECT2000: An improved Monte-Carlo simulator for the computer aided design of photon sensing devices," in *Proc. SPIE 4833*, 2003, p. 69.

[8] J. Graeme*, Photodiode Amplifiers, Op Amp Solutions*. Boston, MA: McGraw-Hill, 1996.